ADVANCED ENERGY MATERIALS
www.advenergymat.de

A High Potential, Low Capacity Fade Rate Iron Complex Posolyte for Aqueous Organic Flow Batteries

Jinxu Gao, Kiana Amini, Thomas Y. George, Yan Jing, Tatsuhiro Tsukamoto, Dawei Xi, Roy G. Gordon, and Michael J. Aziz**

An iron complex, tris(4,4′-bis(hydroxymethyl)-2,2′-bipyridine) iron dichloride is reported, which operates at near-neutral pH with a redox potential of 0.985 V versus SHE. This high potential compound is employed in the posolyte of an aqueous flow battery, paired with bis(3-trimethylammonio) propyl viologen tetrachloride in the negolyte, exhibiting an open-circuit voltage of 1.3 V at near-neutral pH. It demonstrates excellent cycling performance with a low temporal capacity fade rate of 0.07% per day over 35 days of cycling. The extended cycling lifetime is the result of low permeability and improved structural stability of the newly developed iron complex compared to that of the iron tris(bipyridine) complex. The combination of high redox potential and low capacity fade rate compares favorably with those of all previously demonstrated organic and organometallic aqueous posolytes. Extensive investigation into the possible degradation mechanisms, including post-mortem chemical and electrochemical analyses, indicates that stepwise ligand dissociations of the iron complex are responsible for the reported capacity loss during cell cycling. This investigation provides unprecedented insight to guide further improvements of such metalorganic compounds for energy storage and conversion applications.

1. Introduction

With the massive environmental issues and economic costs imposed by consumption of fossil fuels, the utilization of clean energy has become a priority for the global economy.[1] Renewable energy sources such as solar and wind are clean, inexhaustible and rapidly growing. However, the intermittency of these renewable resources limits the depth to which they may penetrate and dominate the energy mix.[2] The development of safe and efficient energy storage technologies could maximize the benefits of large-scale application of renewable energy sources.[3]

Designed for large-scale energy storage with long operational lifetimes[4] and long discharge durations at rated power,[3] aqueous redox flow batteries (ARFBs) have drawn substantial attention due to their inherent fire-safety and potential for cost-effective mass production.[4,5] Over the past decade, many redox-active inorganics, organics and metalorganics have been studied for ARFBs, including but not limited to iron,[6] chromium,[7,8] and vanadium ions,[7,9] quinones,[10–14] aza-aromatics,[15–17] viologens,[15,18–20] nitroxide radicals,[21] and iron complexes.[15,17,22–24]

Iron-based redox-active materials can have cost and environmental advantages when used in redox flow batteries. In the past few years, considerable progress has been made on the development of posolytes composed of iron complexes. The Fe^{2+}/Fe^{3+} redox couple was used as the posolyte species in an iron-chromium redox flow battery with an acidic supporting medium.[7] In spite of the high redox potential of iron (0.77 V vs SHE), the widespread deployment and market penetration of iron-chromium ARFBs was hindered by slow electrochemical kinetics, poor stability and high crossover through the membrane.[7,25] It has been known that organic ligands, such as ethylenediaminetetraacetate ($EDTA^{4-}$), 2,2′-bipyridine (bpy) and cyanide (CN^-), can coordinate with iron ions to form stable and soluble redox-active species.[22,23,26] Among all these redox-active iron complexes, ferri-/ferrocyanide ($[Fe(CN)_6]^{3-/4-}$) is the most commonly used posolyte redox species due to its low cost, non-toxicity and cycling stability at neutral or basic pH.[11,12,26–29] However, the low redox potential (0.45 V vs SHE) of ferri-/ferrocyanide prevents the ARFB system from achieving high overall cell voltage, and its limited solubility provides additional limitations to the energy density. To improve the redox potential of the posolyte within the electrochemical window of water, attention has turned to the ferrocene derivatives involving low-cost starting materials. The ferrocene compound's redox potential has been synthetically tuned to 0.61 and 0.86 V versus SHE by introducing ammonium and sulfonate groups, respectively, for ARFB applications.[17,30]

In recent years, the tris(bipyridyl)iron complex has been used, due to its high redox potential, as the redox-active species of posolytes in both non-aqueous redox flow batteries (1.25 V vs Ag/AgCl in a solution of 0.5 M $TEABF_4$ in propylene

J. Gao, Y. Jing, T. Tsukamoto, R. G. Gordon
Department of Chemistry and Chemical Biology
Harvard University
12 Oxford Street, Cambridge, MA 02138, USA
E-mail: gordon@chemistry.harvard.edu
K. Amini, T. Y. George, D. Xi, R. G. Gordon, M. J. Aziz
Harvard John A. Paulson School of Engineering and Applied Sciences
29 Oxford Street, Cambridge, MA 02138, USA
E-mail: maziz@harvard.edu
The ORCID identification number(s) for the author(s) of this article can be found under https://doi.org/10.1002/aenm.202202444.

DOI: 10.1002/aenm.202202444

carbonate)[31] and ARFBs (1.03 V vs SHE in 1 M NaCl aqueous solution).[32] First investigated as a sensitizing dye for solar cells,[33] $Fe(Dcbpy)_2(CN)_2^{4-/3-}$, an iron complex with the combination of both 2,2′-bipyridine-4,4′-dicarboxylate ($Dcbpy^{2-}$) and cyanide (CN^-) ligands, demonstrated a redox potential of 0.86 V versus SHE[24] for 43.7 days (6000 cycles) with a capacity fade rate of 0.217% per day (0.00158% per cycle).[24] However, the generation of poisonous and flammable hydrogen cyanide gas during synthesis might be a major hinderance to mass production of this iron complex. Thus, the discovery of an electrochemically stable and high-potential posolyte with an environmentally benign synthetic method enables the production of safe and high-performance ARFBs.

Here, we report a near-neutral pH ARFB utilizing a newly designed metalorganic posolyte redox species, tris(4,4′-bis(hydroxymethyl)-2,2′-bipyridine) iron dichloride ($Fe(Bhmbpy)_3$, where Bhmbpy represents 4,4′-bis(hydroxymethyl)-2,2′-bipyridine), with a redox potential of 0.985 V versus SHE, paired with bis(3-trimethylammonio) propyl viologen tetrachloride (BTMAP-Vi) as the negolyte redox species.[15] The BTMAP-Vi | $Fe(Bhmbpy)_3$ ARFB system demonstrates a high open-circuit voltage (1.3 V), an excellent cycling performance with a capacity fade rate of 0.07% per day, and a peak galvanic power density exceeding 120 mW cm^{-2}. Moreover, the crossover rate of this new iron complex is suppressed, which is important to achieve a long-lifetime of ARFB, due to the increased size of the metalorganic complex in comparison to the iron tris(bipyridine) complex. Additionally, molecular decomposition mechanisms are proposed based on extensive post-mortem analyses of the BTMAP-Vi | $Fe(Bhmbpy)_3$ cell. Overall, our study demonstrates the possibility of tuning the electrochemical properties of iron-based metalorganic complexes by structural modification to achieve stable and high-potential redox active species for sustainable energy storage and conversion applications.

2. Results and Discussion

2.1. Molecular Engineering of Ligands for Iron-Based Complexes

By introducing electron-withdrawing groups (EWGs) or electron-donating groups (EDGs) to ligands, the redox potentials of iron complexes can be increased or decreased, respectively. In addition, the solubility can be increased by introducing water-solubilizing groups such as hydroxyls,[11] ammonium groups,[15,17,20] phosphonates,[16,34] carboxylates, sulfonates,[35] and polyethylene glycol (PEG).[19] Through ligand functionalization, this study seeks to investigate iron complexes with rationally designed 2,2′-bipyridine (bpy) derivatives (**1–6**) to achieve a high redox potential and a high stability in aqueous solvents. The structures of iron-bipyridyl complexes synthesized in this study are shown in **Figure 1**a. The detailed synthetic procedures and ^1H- and ^{13}C-NMR spectra of the iron complexes are given in Figures S15–S24 (Supporting Information). The installation of EDGs, such as $-O^-$, $-OCH_3$, $-CH_3$ and $-CH_2OH$ groups, to the bipyridine ligand results in the upfield shift of bpy proton resonances for compounds **1–4** (between 7.3 and 8.6 ppm) with respect to the parent compound **5** due to the increased electron density of these complexes, whereas the opposite is observed in compound **6** in which an EWG (COO^-) is introduced to the ligand (Figure 1b).

The redox potential differences in various iron-bipyridyl complexes (Figure 1c) arise from the electron-donating or electron-withdrawing effects of the substituent groups, affecting the energies of molecular orbitals of the iron complex[31] and modifying the electrostatic environment of the iron center to electron-rich or electron-deficient, thereby causing a shift to lower or higher redox potentials, respectively. Notably, hydroxymethyl groups ($-CH_2OH$) introduced to the 4,4′-positions of 2,2′-bipyridine slightly decrease the redox potential to 0.985 V versus SHE with respect to parent compound **5** (1.03 V vs SHE), whereas the hydroxy substituents (–OH) directly attached to the same positions shift the redox potential to –0.053 V versus SHE due to the deprotonation ($-O^-$) at the measured pH (Figure 1c). With the enhancement of the substituent's electron-donating ability at the given pH, e.g., $-COO^- < -CH_2OH < -CH_3 < -OCH_3 < -O^-$, the redox potentials of various iron-bipyridyl complex derivatives decrease accordingly (Figure 1c). Among all the iron-bipyridyl complex derivatives, compounds **2**, **3**, **4**, and **6** are promising as candidates for posolyte species in terms of their higher redox potentials, compared to previously reported iron-based posolytes, such as $[Fe(CN)_6]^{3-/4-}$[23] and BTMAP-Fc.[15] However, complexes **2** and **6** exhibit low solubility (Figure 1d), which is undesirable in ARFB applications. In comparison to compound **3** with $-CH_3$ substituents on bipyridine ligands, $Fe(Bhmbpy)_3$ (compound **4**) demonstrates a higher redox potential of 0.985 V versus SHE ($E_{1/2}$) with a peak separation of 73 mV, which is dramatically narrower than the $Fe^{3+/2+}$ peak separation of 578 mV (Figure S1a, Supporting Information). No obvious shifts of redox peaks are shown with increased scan rates (Figure S1b, Supporting Information). The excellent electrochemical characteristics make compound **4** a desirable posolyte active species for an ARFB by providing one of the highest redox potentials among the existing redox-active molecules.[24,32] Compound **4** also shows a solubility of 0.98 M in water, 0.68 M in 1 M NaCl solution and 0.59 M in 1 M KCl solution, which are higher than those of compound **5** (Figure 1d). The improved solubility is attributed to the addition of six hydroxymethyl groups to an iron-bipyridyl complex, which participate in hydrogen bonding with water, thus enhancing the hydrophilicity and solubility of **4** in water.

The structure of compound **4** is further confirmed by single-crystal XRD analysis. 4,4′-bis(hydroxymethyl)-2,2′-bipyridines (Bhmbpy) serve as bidentate ligands to form an hexacoordinated iron (II) complex (Figure 1e). Typical for the low-spin iron (II) complex, the Fe—N bond lengths in the complex cations $Fe(Bhmbpy)_3^{2+}$ are in the range of 1.95–1.98 Å (Figure 1e), which are slightly shorter than those in $Fe(bpy)_3^{2+}$ (1.97–1.99 Å).[36] The introduction of electron-donating groups into bipyridine ligands increases their electron densities and binding affinities to the iron center, strengthening the Fe—N bonds and decreasing bond lengths. The crystallographic information of complex **4** (CCDC number 2165676) are summarized in Tables S1 and S2 (Supporting Information). Because of its high redox potential and solubility, compound **4** was chosen as the best posolyte for further studies among all the iron complexes that we investigated.

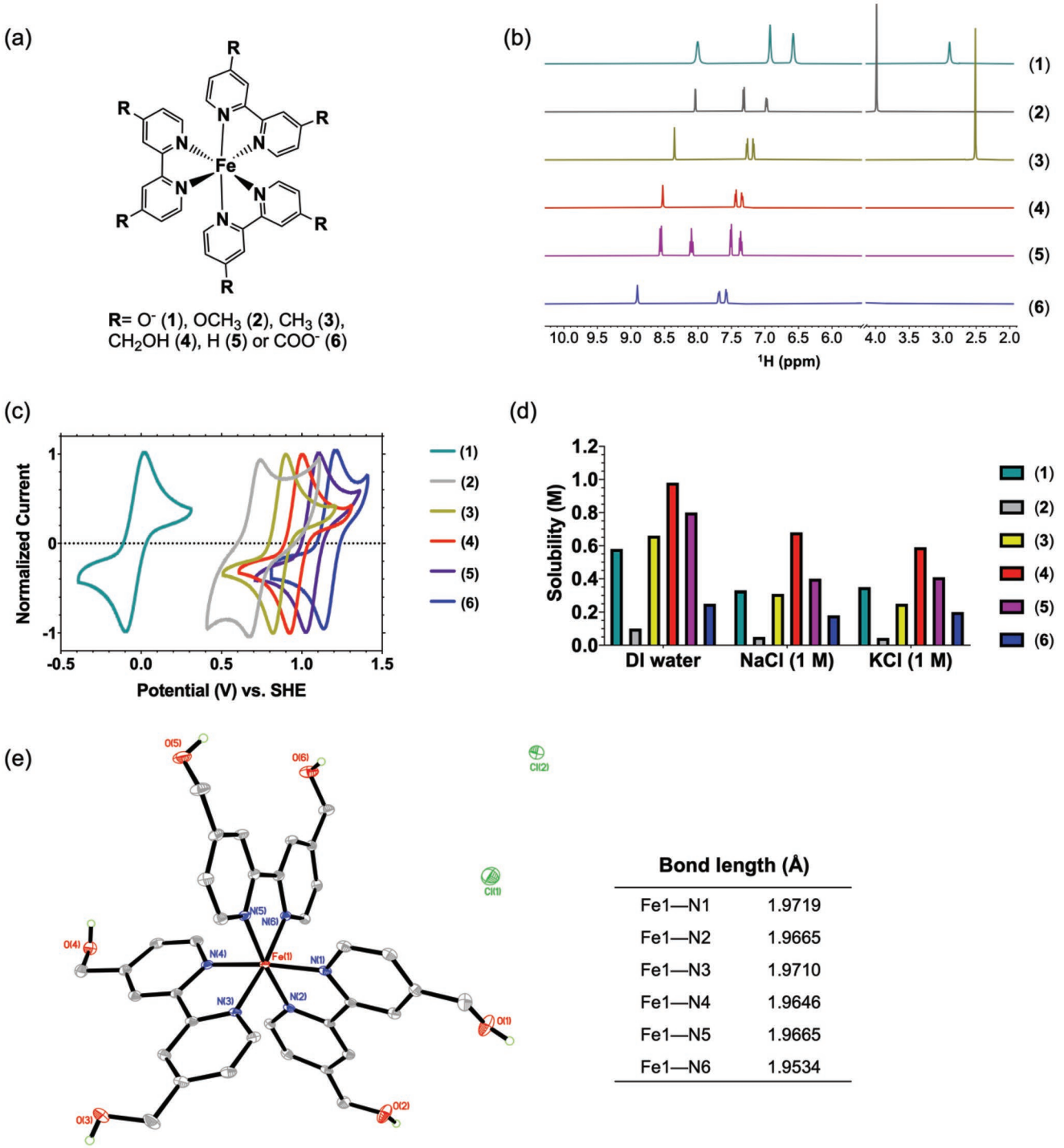

Figure 1. Characterization of iron complexes. a) Chemical structures of iron complexes; CH_2OH stands for ligand Bhmbpy. b) ^{1}H-NMR spectra of iron complexes in D_2O. A break mark was placed from 4.15 to 5.55 ppm to remove the water solvent peak and better present the peaks from the complexes. c) Cyclic voltammograms of 10 mM iron complexes in 1 M NaCl aqueous solution (scan rate 100 mV s^{-1}). The pH values of solutions dissolving iron complexes **2**–**6** were ≈7, whereas the pH value of solution containing complex **1** was adjusted to 12 using 1 M NaOH to dissolve all of the sample by complete deprotonation. The current was normalized in the range of –1 to 1. d) Solubility of iron (II) complexes in deionized (DI) water, 1 M NaCl, and 1 M KCl aqueous solutions. The pH values of solvents for dissolving complex **1** were adjusted to 12. e) Single-crystal X-ray diffraction (XRD) measurement for the structure with atom numbering scheme and selected geometric parameters (bond length) of $Fe(Bhmbpy)_3$ (**4**). Displacement ellipsoids are drawn at the 50% probability level.

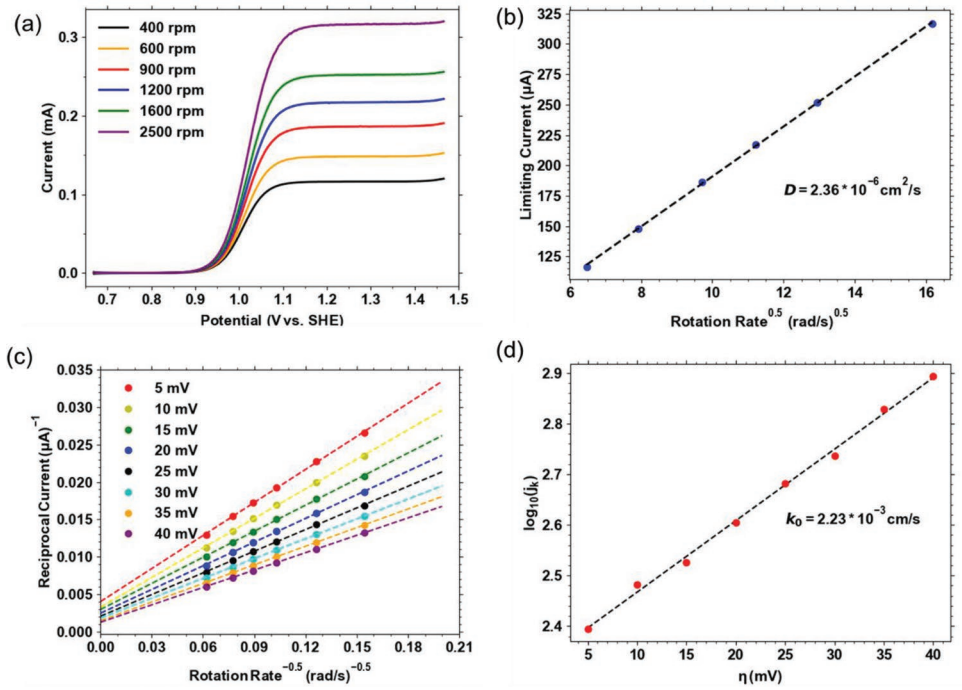

Figure 2. Rotating-disk-electrode experiment on 5 mM $Fe(Bhmbpy)_3$ (**4**) in 1 M NaCl solution. a) Linear sweep voltammograms on a glassy carbon rotating disk electrode at rotation rates between 400 and 2500 rpm with potential sweeping rate of 20 mV s^{-1}. b) Levich plot of limiting current versus square root of rotation rate. c) Koutecký–Levich plot (reciprocal current vs inverse square root of rotation rate) plot of 5 mM $Fe(Bhmbpy)_3$ in 1 M NaCl solution at different overpotentials. d) Fitted Tafel plot of 5 mM $Fe(Bhmbpy)_3$ in 1 M NaCl solution.

2.2. Electrochemical Kinetics

The diffusion coefficient (D) of $Fe(Bhmbpy)_3$ (compound **4**) was measured using rotating disk electrode voltammetry and calculated using the Levich equation to fit the limiting current under various rotation rates (**Figure 2**a). The limiting current increases linearly with the square root of the rotation rate (Figure 2b), indicating that the rate of the oxidation reaction is governed by mass transport to the electrode surface. The diffusion coefficient of the reduced species is 2.36×10^{-6} cm^2 s^{-1}, which is comparable with those of reported iron complexes, such as $K_4[Fe^{II}(CN)_6]$,[23] BTMAP-Fc,[15] and $Na_4[Fe^{II}(Dcbpy)_2(CN)_2]$[24] (Table S7, Supporting Information), which is promising to build a high-current-density ARFB system. Plotting the reciprocal current versus the reciprocal square root of the angular rotation rate yields a straight line (Figure 2c), the intercept of which is the reciprocal kinetic current ($1/j_k$). A plot of the logarithm of the kinetic current (j_k) versus overpotential was used to determine the rate constant (k^0) for the charge transfer of $Fe(Bhmbpy)_3$ (Figure 2d). The slope of the fitted Tafel plot yielded a rate constant of 2.23×10^{-3} cm s^{-1} which, although lower than kinetic rate constants of ferrocyanide[23] and BTMAP-Fc,[15] is comparable to those of other organic reactants used in ARFBs such as 9,10-anthraquinone-2,7-disulphonic acid (AQDS)[10] and 2,6-dihydroxyanthraquinone (2,6-DHAQ),[11] and is much greater than those of inorganics including V^{3+}/V^{2+}[37] and Fe^{3+}/Fe^{2+}.[38] This suggests much smaller kinetic overpotentials under the same conditions. All the electrochemical data for compound **4** and other reported electrolytes for comparison are summarized in Table S7 (Supporting Information).

2.3. Flow Battery Performance

We assembled a near-neutral pH ARFB, with a posolyte composed of $Fe(Bhmbpy)_3$ and a negolyte composed of BTMAP-Vi, separated by a Selemion DSV-N anion-exchange membrane, which delivered a working voltage of 1.3 V (**Figure 3**a). The corresponding redox reactions and potentials are shown in Equations (1) and (2) in Scheme S1b (Supporting Information). During the discharging process, electrons are withdrawn from BTMAP-Vi in the negolyte, and flow along the external circuit to $Fe(Bhmbpy)_3$ in the posolyte, while the Cl^- ions migrate across the anion exchange membrane as the internal charge carrier (Figure 3b). For comparison, $Fe(bpy)_3$ (compound **5**) was used as the posolyte active species pairing with BTMAP-Vi at the same electrolyte concentration.

Figure 3c demonstrates an increase in the open circuit voltage (OCV) of the battery from 1.2 V at 10% state of charge (SOC) to 1.36 V at 90% SOC. The high frequency area-specific resistance (ASR) of the battery is slightly over 1.2 Ω cm^2 across all SOC ranges due to the membrane resistance. The polarization resistance varies from 2.55 to 2.85 Ω cm^2, indicating that about 45% of the total resistance of the cell can be attributed to the constant membrane resistance. The remaining ≈55% of the total resistance is attributed to the kinetic losses associated with the reduction of the ferric complex as well as dimerization, which will be discussed in the mechanism section. From polarization curves at varied SOC (Figure 3d), $Fe(Bhmbpy)_3$ delivers a peak power density of 120 mW cm^{-2} at 90% SOC and 100 mW cm^{-2} at 50% SOC. Galvanostatic charging and discharging of the battery at different applied current densities

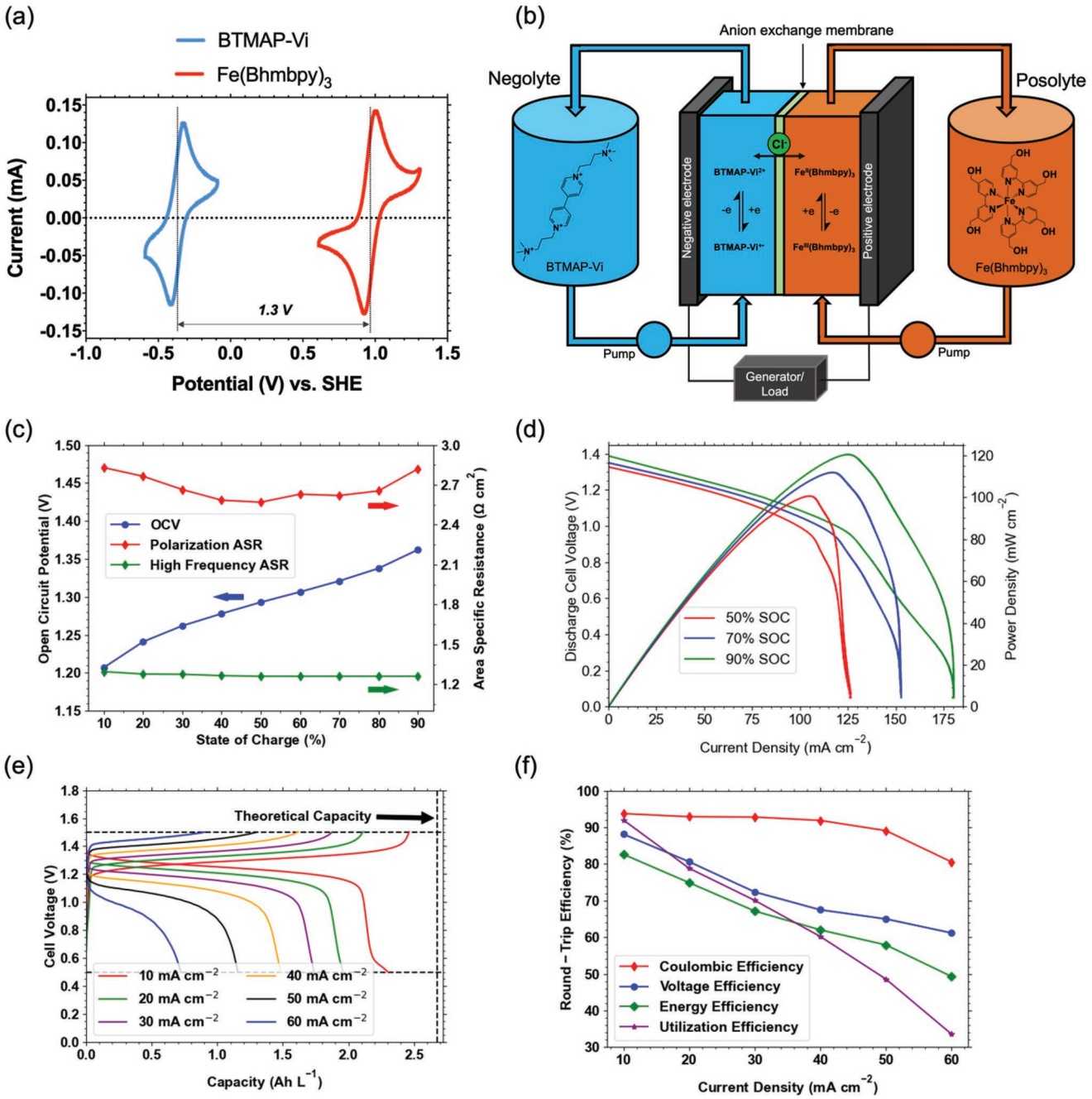

Figure 3. A near-neutral pH ARFB with a $Fe(Bhmbpy)_3$ posolyte and a BTMAP-Vi negolyte. a) Cyclic voltammograms of $Fe(Bhmbpy)_3$ (red trace) and BTMAP-Vi (blue trace). The electroactive compounds were tested at 10 mM in 1 M NaCl solution at a scan rate of 100 mV s^{-1}, on a glassy carbon working electrode. b) Schematic configuration of the BTMAP-Vi | $Fe(Bhmbpy)_3$ ARFB and illustrations of discharged and charged states of posolyte and negolyte and cell reactions, with chloride ions passing through a Selemion DSV-N anion exchange membrane. c) Plots of OCV and high frequency and polarization ASR versus SOC for ARFB assembled with 0.1 M $Fe(Bhmbpy)_3$ in 1 M NaCl solution as the posolyte (≈4.9 mL) and BTMAP-Vi in 1 M NaCl solution as the negolyte (30 mL, 0.06 M oxidized BTMAP-Vi, 0.01 M singly reduced BTMAP-Vi), with Selemion DSV-N as the anion exchange membrane. The cell cycling tests were conducted in a N_2-filled glove box. The capacity is presented in units of ampere-hours per liter of posolyte. d) Cell voltage and power density during discharge at various SOC. e) Galvanostatic charge–discharge curves at various current densities (10, 20, 30, 40, 50, and 60 mA cm^{-2}) with 1.5 and 0.5 V cutoffs. The theoretical capacity is indicated by the vertical dashed line. f) Coulombic, voltage, energy, and electrolyte utilization efficiencies at different applied current densities. The cell cycling condition for (d), (e), and (f) is as the same as that in (c).

was conducted to extract the accessed capacity and the resulting round-trip efficiencies. As shown in Figure 3e,f, under the constant current galvanostatic protocol, lower capacity and lower utilization are accessed at higher current densities due to higher ohmic resistances and mass transport overpotentials in the system. The larger overpotentials at higher applied current

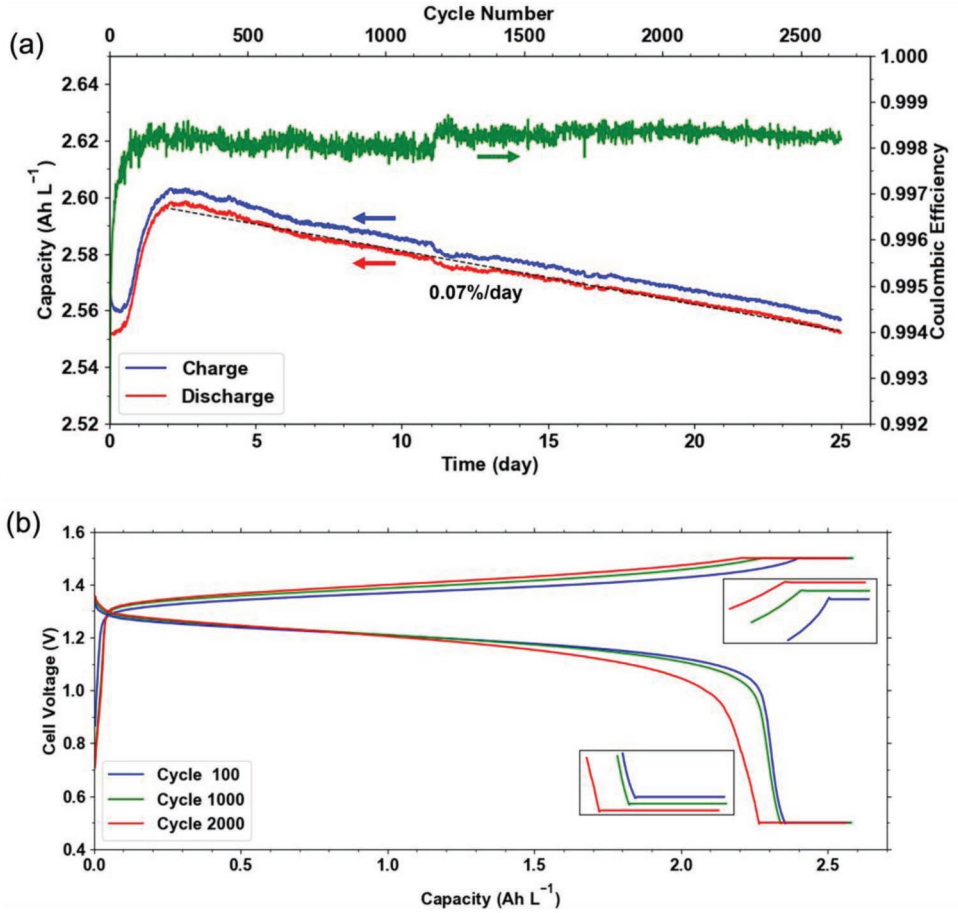

Figure 4. Cell cycling of a near-neutral ARFB assembled with 0.1 M $Fe(Bhmbpy)_3$ in 1 M NaCl solution as the posolyte (≈4.9 mL) and BTMAP-Vi in 1 M NaCl solution as the negolyte (30 mL, 0.06 M oxidized BTMAP-Vi, 0.01 M singly reduced BTMAP-Vi), with Selemion DSV-N as the anion exchange membrane. The cell cycling tests were conducted in a N_2-filled glove box. The capacity is presented in units of ampere-hours per liter of posolyte. a) Charge and discharge capacities and coulombic efficiency versus time and cycle number operating with a constant current (30 mA cm^{-2}) followed by constant potentials of 1.5 V (charging) and 0.5 V (discharging) during 25 days of operation. The dashed line shows the starting and the end date used for calculation of the capacity fade rate. b) Charge–discharge voltage–capacity profiles of $Fe(Bhmbpy)_3$ from selected cycles in (a). Inset traces are vertically offset from each other for clarity.

densities results in lower voltage efficiencies as depicted in Figure 3f. The majority of the losses in the round-trip energy efficiency are rooted in the voltage efficiency losses in the battery.

Figure 4a depicts the charge–discharge capacities as well as the coulombic efficiency of the battery operated with a constant current (30 mA cm^{-2}) followed by constant potentials of 1.5 V (charging) and 0.5 V (discharging) during 25 days of operation. The battery capacity initially increased during the first day of operation reaching the maximum capacity of 2.60 Ah L^{-1} or 55.2 C, corresponding to 97% of the theoretical capacity. The small difference (less than 5%) between realized capacity and the theoretical value could come from errors in electrolyte volume measurement or the presence of redox-inactive impurities. The voltage–capacity profiles of the battery at three different cycle numbers with the chosen cut-off values are shown in Figure 4b. After 25 days of full SOC range cycling, the temporal capacity fade rate of the battery was 0.07% per day or 0.00077% per cycle. The battery continued operation beyond 25 days. On day 27, the non-capacity limiting side (BTMAP-Vi) was refreshed to compensate for the SOC imbalance accumulating in the battery. As shown in Figure S2 (Supporting Information), the capacity was recovered, and a temporal fade rate of 0.08% per day was observed over the following 10 days of operation, demonstrating the consistency of our fade rate measurements.

In order to further understand the role of hydroxymethyl functionalization on the stability and performance of the redox active species, the performance of the cell operated with $Fe(Bhmbpy)_3$ (compound **4**) is compared to a cell with $Fe(bpy)_3$ (compound **5**), a tris(bipyridyl)iron complex previously tested in a flow battery.[32] Figure S3a (Supporting Information) depicts the charge–discharge capacities as well as the charge efficiency of the battery during 5 days of operation. The voltage–capacity profiles of the battery at three different cycle numbers with the chosen cut-off values are shown in Figure S3b (Supporting Information). After five days of full SOC range cycling, the temporal capacity fade rate of the BTMAP-Vi | $Fe(bpy)_3$ cell was 0.6% per day or 0.006% per cycle, which is almost 10 times higher than the capacity fade rate of the BTMAP-Vi

| $Fe(Bhmbpy)_3$ cell (0.07% per day) (Figure S3c, Supporting Information). We attribute the cycling lifetime extension of the BTMAP-Vi | $Fe(Bhmbpy)_3$ cell to the bond strengthening between the hydroxymethyl-functionalized bipyridine ligand and iron center in compound **4**, compared to weaker bond strength between non-functionalized bipyridine and iron in compound **5**,[36] thus improving the stability of the newly developed compound **4**.

To further investigate cycling performance at a higher concentration, we constructed a cell with ≈5.0 mL of 0.5 M $Fe(Bhmbpy)_3$ in DI water (capacity-limiting side) paired with 27 mL of 0.46 M BTMAP-Vi in DI water (Figure S4, Supporting Information) operated under the same protocol described for the battery test at 0.1 M. After 7 days of full range cell cycling, a temporal fade rate of 0.16% per day and cycle-denominated fade rate of 0.006% per cycle were observed, which are larger fade rates compared to those at low concentrations of $Fe(Bhmbpy)_3$. To unravel the sources of capacity fade of this posolyte at low and high concentrations, we report an extensive investigation of the possible degradation mechanisms in the next section.

2.4. Degradation Mechanism Investigation

In the pursuit of a high-performing and long-lasting flow battery, understanding the capacity fade mechanism is of great importance.[39,40] Irreversible capacity fade in ARFBs can be attributed to active species crossover through the membrane[41,42] or their decomposition.[39] In this study, several post-mortem analysis techniques including electrochemical methods, NMR, and mass spectrometry are deployed to unravel the capacity decay mechanisms.

To explore the time-dependent degradation mechanisms of $Fe(Bhmbpy)_3$, we used the same 0.1 M flow cell for self-discharge characterization. In this characterization, the cell was first operated normally for 5 cycles with the discharging phase immediately following the charging phase with no wait time. Consequently, the battery was cycled for 5 cycles with 20 min wait duration at the fully charged state (stopped at 100% SOC) before the discharging phase began. During this wait time, the battery was at open circuit. No such pause occurred in the fully discharged state. The same protocol was repeated for 30 min, 1 h, and 5 h wait durations after the charging phase. In all cycles, the cell was tested at a constant current of 30 mA cm^{-2}, followed by a constant charging voltage of 1.5 V and discharging voltage of 0.5 V until the current dropped to 1 mA cm^{-2}. **Figure 5**b demonstrates the discharge capacity versus cycle number for this protocol. We observe that for longer wait durations at 100% SOC, the extracted capacity during the discharge process is lower. In other words, during the wait time, some of the oxidized form of $Fe(Bhmbpy)_3$ (depending on the duration of hold) self-discharged and hence we can no longer extract the capacity during the discharge process. Thus, the coulombic efficiency of the battery dropped for the cycles containing wait times. Note that when the protocol was switched to normal cycling with no hold at 100% SOC, the initial capacity was again recovered, and the coulombic efficiency rose back to nearly 100% (Figure 5c). This behavior suggests that the oxidized form of compound **4** self-discharges to the reduced form, instead of converting irreversibly to another non-redox active species. This observation is also consistent with the thermal stability tests shown in Figure S6 (Supporting Information), where, after a week of electrolyte storage at elevated temperature (65 °C), we detected increased concentration of the reduced, ferrous complex in the initially charged ferric complex solution, demonstrating a chemical conversion of the ferric complex to the ferrous complex. Ex situ UV–vis absorption spectra of fully charged posolytes over time also support this finding, demonstrating that $Fe(Bhmbpy)_3^{3+}$ gradually becomes reduced over time during self-discharge (Figure S14, Supporting Information). Additionally, the final pH value of the solution after self-discharge in the battery dropped to ≈3 from the initial pH which was close to the neutral condition, suggesting the generation of protons (**Scheme 1**, route 2). When the pH value of the electrolyte drops to ≈3, the ligand exists mainly as the singly protonated form of Bhmbpy, i.e., $H(Bhmbpy)^+$, because the pKa_2 of $H_2(Bhmbpy)^{2+}$ is 4.2. At neutral pH values, the oxygen evolution potential is lower than that of the Bhmbpy compound and hence self-discharge supported by oxygen evolution is possible. This spontaneous self-discharge phenomenon has also been recently reported for ferri-/ferrocyanide as the electroactive component.[43] Nevertheless, the oxygen evolution potential at pH 3 is 1.04 V versus SHE, which is higher than 0.985 V, which is the redox potential of the ferric complex; hence the self-discharge of ferric complex supported by oxygen evolution is thermodynamically unfavorable when the pH drops to lower values than neutral (≈pH 3) during the cycling. Because of the generation of protonated Bhmbpy ligands during dimerization of ferric complex (Scheme 1, route 1), we propose that the self-discharge of the oxidized $Fe(Bhmbpy)_3$ can also be facilitated by the oxidation of protonated Bhmbpy (Scheme 1, route 2).[44,45] The m/z value of 233.0921 was found in the cycled posolyte solution by mass spectrometry (Figure S33b, Supporting Information), which is consistent with the m/z of the protonated 4,4′-bis(hydroxymethyl)-2,2′-bipyridine *N*-oxide [$H(Bhmbpy\text{-}O)^+$]. Additionally, we observed that the addition of 20 mM of the protonated ligand to the battery posolyte results in a larger drop in the battery's coulombic efficiency during the wait time experiment (Figure S37, Supporting Information), which corroborates our proposed self-discharge mechanism (Scheme 1, route 2).

Figure 5a,c shows the cell voltage versus capacity and coulombic efficiency versus cycle number, respectively, indicating that the coulombic efficiency and accessed discharge capacity decrease slightly with longer durations of hold time at 100% SOC. Interestingly, the discharge voltage profile dropped to the constant voltage phase earlier with longer hold durations (5 h), providing the majority of the discharge capacity at the lower constant voltage of 0.5 V. This observation is consistent with our proposed mechanism (Scheme 1, route 1), where the oxidized complex undergoes dimerization. The dimer is electrochemically active (Figure S5b, Supporting Information) and is reduced back to the ferrous complex at a lower reduction potential (Scheme 1, route 3). Consequently, with longer hold durations, dimerization increases and, hence, a larger portion of the discharge process occurs at the lower potential of 0.5 V. Note that after changing the protocol to the normal cycling (with zero wait time), we no longer observed the early drop of the voltage

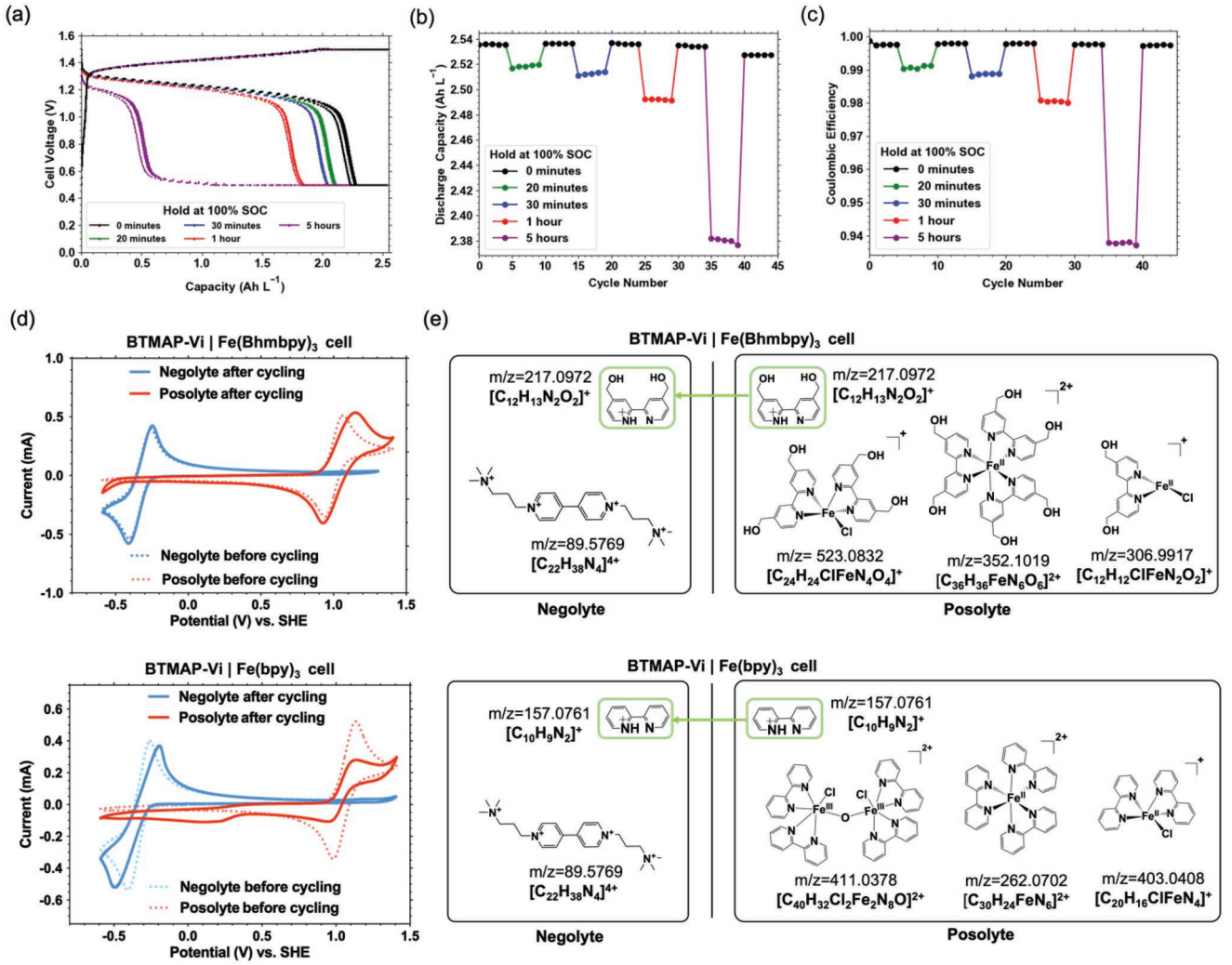

Figure 5. Post-cycling analysis for BTMAP-Vi | Fe(Bhmbpy)$_3$ and BTMAP-Vi | Fe(bpy)$_3$ cell. a) Cell voltage versus discharge capacity for self-discharge characterization of BTMAP-Vi | Fe(Bhmbpy)$_3$ cell, consisting of intervals (5 cycles) in which, after the charging phase (at 100% SOC), the battery was held at open circuit potential for durations of 20 min, 30 min, 1 h, and 5 h. Between each interval, the battery was operated normally with a discharging phase immediately following the charging phase with no hold duration (0 wait time). Discharge capacity b) and coulombic efficiency c) versus cycle number for self-discharge study for Fe(Bhmbpy)$_3$ after charging at 100% SOC, followed by holding at open circuit potential for durations of 20 min, 30 min, 1 h, and 5 h. Between each interval, the battery was operated normally with discharging phase immediately following the charging phase with no hold duration (0 wait time). d) Cyclic voltammograms of the negolytes and posolytes before and after cycling for ARFBs using Fe(Bhmbpy)$_3$ and Fe(bpy)$_3$ in the posolyte, respectively. The dash line indicates CV before cycling, and the solid line indicates CVs after cycling. e) Mass spectrometry analysis after cycling for BTMAP-Vi | Fe(Bhmbpy)$_3$ and BTMAP-Vi | Fe(bpy)$_3$ ARFB.

to the constant value of 0.5 V. Given that the capacity, voltage profile and coulombic efficiency recovered when the protocol was changed to the normal cycling, we conclude that the additional wait time did not accelerate the irreversible decomposition of the compound. Furthermore, based on the recovered capacity at the end of this cell test, the temporal capacity fade rate was 0.08% per day, consistent with the extended cell cycling of the battery (Figure S2, Supporting Information).

The dimerization, however, is responsible for larger capacity fade rate at higher concentration. Although the solubility limit of Fe(Bhmbpy)$_3$ is higher than 0.5 M in 1 M NaCl solution (Figure 1d), we observed formation of small precipitates at the end of battery cycling (Figure S5e, Supporting Information). We propose that the precipitates are due to the dimerization of the oxidized form of the posolyte[46] (Scheme 1, route 1). To investigate the structure of the newly formed precipitate during high-concentration cell cycling, we chemically synthesized the ferric dimer $[Fe_2O(Bhmbpy)_4Cl_2]^{2+}$ (compound **7**) (see Scheme 1) according to a modified synthetic method[36] (see Supporting Information for details) and obtained its single-crystal XRD data (CCDC number: 2165674) for comparison and further analysis (Figure S5d, Tables S3 and S4, Supporting Information). The solubility of the synthesized ferric dimer **7** is 2 mM in 1 M NaCl solution. By comparing the ^{1}H NMR spectra of single-crystal ferric dimer **7** and samples (soluble part and precipitate) from high-concentration cell cycling, we found that the chemical shifts of synthesized ferric dimer **7** are in line with peaks shown in the precipitate (Figure S5a, Supporting Information),

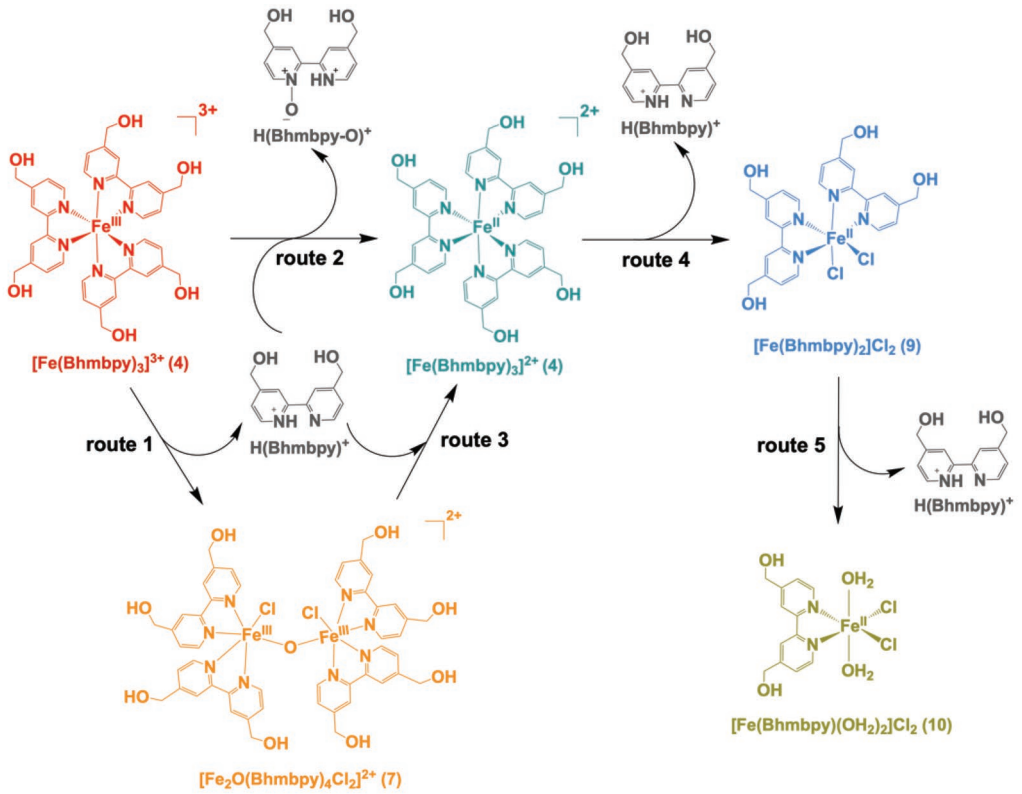

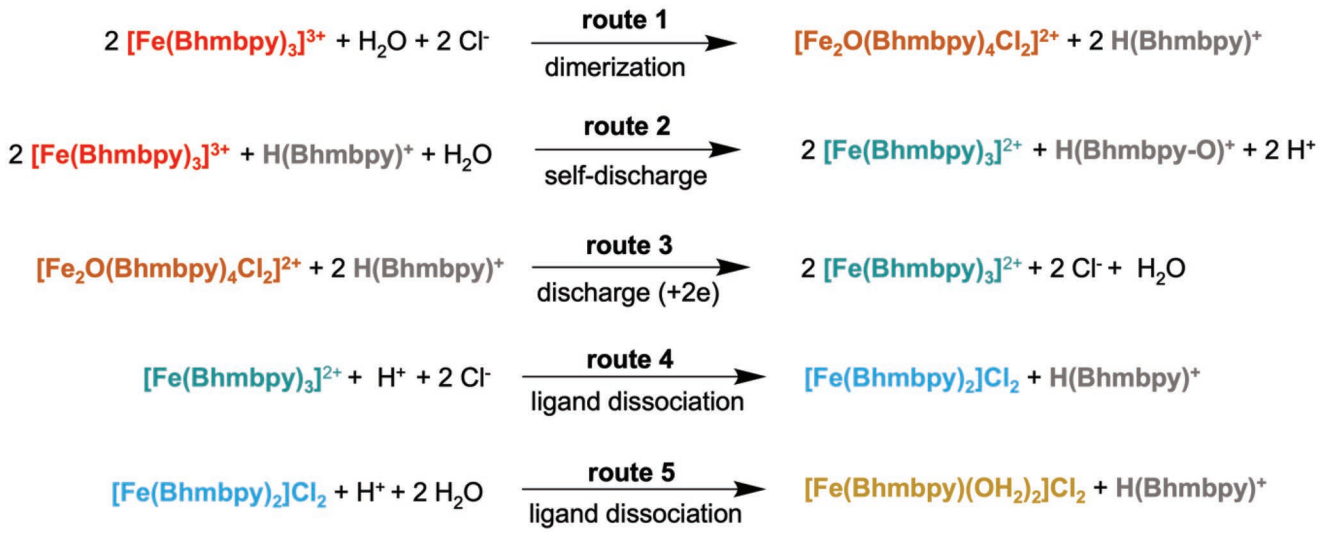

Scheme 1. Proposed decomposition mechanism for $Fe(Bhmbpy)_3$ (compound **4**) during cell cycling. For consistency purposes, we propose all the iron complexes in this mechanism to be six-coordinate.

indicating that the newly formed precipitate is identical to the ferric dimer **7** that we synthesized. The mass spectrometry of precipitate sample also confirms the presence of ferric dimer in high-concentration cell test (Figure S5c, Supporting Information). Moreover, different from the CV of a soluble sample containing $Fe(Bhmbpy)_3^{2+/3+}$, a cathodic peak appears at 0.27 V during the reduction of ferric dimer for both synthesized **7** and precipitate sample (Figure S5b, Supporting Information), demonstrating a potential gap of ≈0.7 V between the new cathodic peak and the cathodic peak of $Fe(Bhmbpy)_3^{2+/3+}$ redox couple, which is consistent with the cell voltage drop in Figure S4b (Supporting Information). This indicates that the higher concentration of oxidized form of $Fe(Bhmbpy)_3$ increases its presumably bimolecular reaction rate and induces the accumulation of the low-solubility ferric dimer, resulting in a higher capacity fade rate at high concentrations than at low concentrations.

Likewise, we employed the same protocol to explore whether additional degradation mechanism, i.e., self-discharge or dimerization, are present with $Fe(bpy)_3$ (compound **5**). Similar to the case of $Fe(Bhmbpy)_3$, both self-discharge and dimerization were observed with $Fe(bpy)_3$. As shown in Figure S8a (Supporting Information), for longer wait durations at 100% SOC, the extracted capacity during the discharge process was lower, which results in lower coulombic efficiency due to self-discharge (Figure S8b, Supporting Information). Additionally, with longer hold durations, the discharge voltage profile dropped to the constant voltage phase earlier (Figure S8c, Supporting Information), providing the majority of the discharge capacity at the lower constant voltage of 0.5 V, which is due to the formation of ferric dimer of posolyte active species.[46] Notably, the full cell voltage dropped by ≈0.7 V, which is consistent with the potential difference between $Fe(bpy)_3^{2+/3+}$ and the newly appearing cathodic peak of synthesized ferric dimer **8** (Figure S8e, Supporting Information, single-crystal data are shown in Tables S5 and S6, Supporting Information, CCDC number: 2165675) shown at 0.27 V versus SHE (Figure S8d, Supporting Information), indicating that dimerization occurs in the fully charged state with longer hold durations. Although dimerization of the tris(bipyridyl)iron complex has previously been reported,[32,46] the self-discharge phenomena has not been identified, given that commonly used characterization techniques comprise cycling with immediate charge/discharge phases without hold time. Our results show that at least for redox active compounds with highly positive reduction potentials, the possibility of self-discharge needs to be explored as part of the characterization method.

The extended cell cycling tests were analyzed by ex situ cyclic voltammetry. Figure 5d and Figure S9a (Supporting Information) show the cyclic voltammetry of the $Fe(Bhmbpy)_3$ electrolyte (cycled for more than 35 days) using a glassy carbon disk electrode and carbon fiber ultramicroelectrode, respectively, in comparison with the fresh (as-prepared) $Fe(Bhmbpy)_3$ compound. The same comparison is also provided for the compound **5** (cycled for 5 days) and the fresh solution before cycling (Figure 5f and Figure S9b, Supporting Information). Both cycled electrolytes were taken out of the cell after full discharge (0% SOC). Whereas the fully discharged solutions of $Fe(Bhmbpy)_3$ showed no new peaks (Figure 5d), clear reduction peaks were found in the cycled solution of compound **5** at 0.26 V versus SHE (Figure 5f), depicting the accumulation of dimers in the posolyte after extended cycling.

To further study possible decomposition of redox-active electrolytes during cell cycling, the cycled samples including posolyte and negolyte of both BTMAP-Vi | $Fe(Bhmbpy)_3$ and BTMAP-Vi | $Fe(bpy)_3$ cell were analyzed by mass spectrometry (Figure S10, Supporting Information). The raw mass spectrometry data and theoretical isotopic pattern are shown in Supporting Information. Notably, ferric dimer consisting of two Fe^{III} atoms and a bridge oxygen atom was not found in cycled BTMAP-Vi | $Fe(Bhmbpy)_3$ cell, suggesting a negligible amount of the dimer remains in the fully reduced ferrous complex after 35-day cycling followed by fully discharging the posolyte. Although dimerization occurs while charging, complete discharge during cell cycling reverses the dimerization (Scheme 1, route 3), avoiding irreversible capacity loss. Instead, two new singly charged ions (m/z = 523.0832 for $[C_{24}H_{24}ClFeN_4O_4]^+$ and m/z = 306.9917 for $[C_{12}H_{12}ClFeN_2O_2]^+$) and charged ligand ($m/z$ = 217.0973 for $[C_{12}H_{13}N_2O_2]^+$) were found by mass spectroscopy (Figures S32, S35, and S33a, Supporting Information). This is associated with ligand release from the iron center caused by pH decrease during cycling (Scheme 1, route 4 and 5).

In contrast to the BTMAP-Vi | $Fe(Bhmbpy)_3$ cell, in the posolyte of the cycled BTMAP-Vi | $Fe(bpy)_3$ cell, a charged ferric dimer (m/z = 411.0378 for $[C_{40}H_{32}Cl_2Fe_2N_8O]^{2+}$) was detected (Figure S28, Supporting Information), along with a charged ligand (m/z = 157.0761 for $[C_{10}H_9N_2]^+$, Figure S30a, Supporting Information) and a singly charged ion (m/z = 403.0408 for $[C_{20}H_{16}ClFeN_4]^+$, Figure S29, Supporting Information). This reveals that a considerable amount of ferric dimer is generated during the cycling of BTMAP-Vi | $Fe(bpy)_3$ cell, which is difficult to convert back to $Fe(bpy)_3^{2+}$ even with full discharging, thus contributing to the high capacity fade rate of 0.6% per day. Moreover, the presence of protonated ligands in both posolytes and negolytes of cycled cells indicates a possible ligand dissociation during cycling (Figure S12, Supporting Information, route 3), followed by transport of protonated ligands from the posolyte to negolyte side across the membrane, which might also lead to irreversible capacity loss over time. We summarize all the charged ions observed by mass spectrometry in Figure 5e.

To investigate the crossover of the redox-active electrolytes, ^1H NMR spectra, CV and mass spectrometry after cell cycling for both posolyte and negolyte sides were examined. From the post-cycling NMR data (Figure S11, Supporting Information), no peaks of $Fe(Bhmbpy)_3$ or $Fe(bpy)_3$ were observed in the negolyte (BTMAP-Vi) after cycling. The CV and mass spectrometry suggest negligible crossover of both electrolytes through Selemion DSV-N anion exchange membrane (Figure 5d,e). Moreover, no observable $Fe(bpy)_3^{2+}$ (Figure S27, Supporting Information) or $Fe(Bhmbpy)_3^{2+}$ (Figure S31, Supporting Information) was found in cycled negolytes by mass spectrometry, which is in accordance with low permeation rate for both $Fe(Bhmbpy)_3$ and $Fe(bpy)_3$ (Figure S13 and Table S7, Supporting Information). The crossover of redox-active posolyte and negolyte for the BTMAP-Vi | $Fe(Bhmbpy)_3$ cell is negligible, but the protonated ligands dissociated from the complex in the posolyte over cycling (Scheme 1, route 1, 4 and 5; Figure S12, Supporting Information, route 1 and 3) crossed over to the negolyte side through the membrane, which is responsible for the capacity fade during cycling.

Considering all the above points regarding our degradation mechanism analysis, we found that for the BTMAP-Vi | $Fe(Bhmbpy)_3$ cell, the dimer forms during cell charging (Scheme 1, route 1) and converts to $Fe(Bhmbpy)_3^{2+}$ during discharging (Scheme 1, route 3). In contrast, the BTMAP-Vi | $Fe(bpy)_3$ cell generates significant amounts of ferric dimers during cell cycling (Figure S12, Supporting Information, route 1) with fewer dimers converting back to $Fe(bpy)_3^{2+}$ (Figure S12, Supporting Information, route 4) or other redox-active species, thus leading to detectable ferric dimers remaining in the fully discharged posolyte and responsible for the capacity fade of the $Fe(bpy)_3^{2+}$ over time. Additionally, the self-discharge phenomenon was confirmed for both $Fe(Bhmbpy)_3^{2+}$ and $Fe(bpy)_3^{2+}$ by

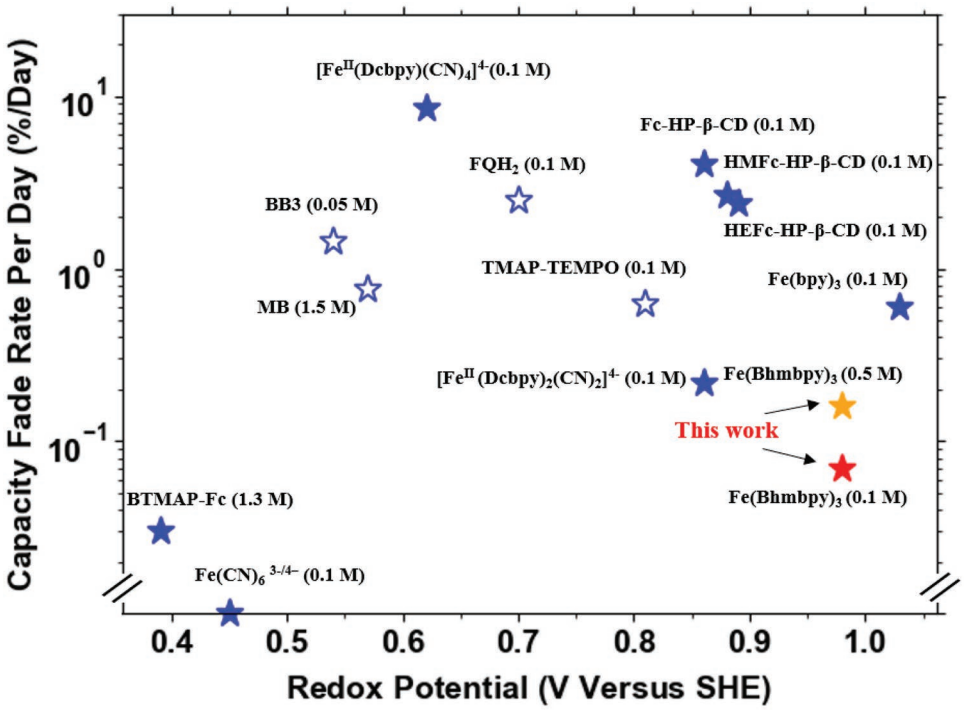

Figure 6. Capacity fade rate per day versus redox potential of previously reported organic and metalorganic posolytes tested as the capacity limiting side of a battery and that of present work. The numbers are taken from refs. [15,21,24,32,43,47–50]. The data for $Fe(bpy)_3$ were obtained from our cell cycling experiments. The $Fe(CN)_6^{3-/4-}$ compound is completely stable at pH 7 and thus is placed on the *x*-axis. Demonstrated capacity fade rates of cells run with potential holds are plotted as filled stars. Apparent capacity fade rates of cells run without potential holds are plotted as hollow stars. Further information regarding these posolytes can be found in Table S8 (Supporting Information).

holding fully charged cells for various time intervals for both posolytes (Scheme 1, route 2; Figure S12, Supporting Information, route 2), which involves the spontaneous chemical reduction of the redox-active electrolytes. Thus, it is not the direct reason for the iron complex decomposition and the corresponding capacity fade.

The $Fe(Bhmbpy)_3$ compound reported in the present work combines two important performance factors for a successful redox active molecule, which is having a low capacity fade rate (0.07% per day) at a large positive redox potential (+0.985 V vs SHE). For comparison, previously reported organic and organometallic redox active molecules evaluated in the positive side of the battery (positive CLS) are shown in **Figure 6**. Although compounds in the lower range of redox potential (0.3–0.5 V vs SHE) show low-capacity fade rate (essentially zero for ferri-/ferrocyanide at pH 7),[43] the respective output cell voltage would be restricted due to their lower redox potential.[15] When comparing compounds with larger redox potential (≥0.5 V vs SHE), the capacity fade rates are one to two orders of magnitude higher than that of $Fe(Bhmbpy)_3$. Even with the dimerization problem at a higher concentration of 0.5 M $Fe(Bhmbpy)_3$, the cell's capacity fade rate is smaller than those previously repo rted.[21,24,32,47–50] Additionally, our extensive post-mortem analysis of the possible degradation mechanisms opens the door for further improvement of $Fe(Bhmbpy)_3$ redox active species. Prevention of dimerization should further improve the performance of the $Fe(Bhmbpy)_3$ in terms of chemical stability and battery cell voltage at high concentrations. The resulting imbalance from the self-discharge of the molecule can be resolved with a rebalancing system.[51] Moreover, the production of protons during the self-discharge and the consequent induced stepwise ligand dissociations can be addressed by pH adjustment or the use of appropriate buffered electrolytes, which should further increase the stability of the compound at all ranges of concentrations. To further improve the volumetric capacity of this system, one potential approach is to introduce water solubilizing groups such as ammonium groups,[15,17,20] phosphonates,[16,34] and sulfonates,[35] to bipyridine ligands; another is to develop electrolyte additives to raise the solubility of redox active compound,[52] which requires the investigation of appropriate additives in the future studies.

3. Conclusion

Six iron tris(bipyridine)-based derivatives were synthesized and characterized in terms of their redox potential and solubility. Among them, tris(4,4′-bis(hydroxymethyl)-2,2′-bipyridine) iron dichloride ($Fe(Bhmbpy)_3$) was studied as the posolyte active species due to its high redox potential and solubility. A flow cell comprising a $Fe(Bhmbpy)_3$ posolyte (0.1 M) and BTMAP-Vi negolyte (0.1 M) separated by a Selemion DSV-N anion-exchange membrane demonstrated a high open-circuit voltage of 1.3 V at near-neutral pH at 50% SOC, delivering a peak power density of 120 mW cm^{-2} at 90% SOC and showing excellent cycling stability with a capacity fade rate of 0.0007% per cycle and 0.07% per day. Post-cycling analysis by mass spectrometry and CV indicated negligible crossover of posolyte

through the membrane, consistent with a low permeation rate of 1.1×10^{-11} cm^2 s^{-1}. We investigated the possible decomposition pathways during cell cycling to an unprecedented level of depth for an aqueous posolyte. We found that the compound degrades through self-discharge, dimerization and ligand dissociation. In comparison with previously reported organic and organometallic compounds, Fe(Bhmbpy)$_3$ exhibits a superior combination of high positive redox potential and low capacity fade rate. The proposed decomposition pathways explain the capacity fade phenomena and offer opportunities for future improvement of metalorganic posolytes with high redox potential and good cycling stability.

4. Experimental Section

Materials and Instrumentation: 1,1′-Bis[3-(trimethylammonio)propyl]-4,4′-bipyridinium Tetrachloride Dihydrate (BTMAP-Vi) was purchased from TCI Chemicals. 2,2′-bipyridine, 4,4′-dimethyl-2,2′-bipyridine and 4,4′-dimethoxy-2,2′-bipyridine were purchased directly from Sigma-Aldrich. Other reagents were purchased from VWR International and used as received unless otherwise stated. ^{1}H- and ^{13}C-NMR spectra were measured on Bruker AVANCE NEO 400 (N400) spectrometer. Electrospray ionization-mass spectrometry (ESI-MS) was conducted on a Bruker Impact HD q-TOF Mass Spectrometer.

Cyclic Voltammetry: Cyclic voltammetry and was recorded by an electrochemical analyzer from CH instruments CHI 608E with a three-electrode system including one glassy carbon working electrode, one platinum counter electrode and one Ag/AgCl reference electrode. The glassy carbon working electrode was polished with an aluminum slurry before and after each scan.

Rotating Disk Electrode (RDE): Rotating disk electrode (RDE) tests were performed using a Pine Instruments Modulated Speed Rotator AFMSRCE equipped with a 5 mm diameter glassy carbon working electrode (Pine Instruments E5PK), an Ag/AgCl reference electrode in 3 M NaCl solution (CHI), a graphite counter electrode and a Gamry Reference 3000 potentiostat.

Prolonged Cell Cycling: The long-term cycling performance of Fe(Bhmbpy)$_3$ was analyzed in a cell compromised of ≈5.9 mL 0.1 M Fe(Bhmbpy)$_3$ in 1 M NaCl paired with 40 mL of 0.06 M BTMAP-Vi (oxidized)/0.01 M BTMAP-Vi (reduced) in 1 M NaCl. Excess capacity is used in the negolyte to ensure that the posolyte side with Fe(Bhmbpy)$_3$ is the capacity limiting side of the cell. The two half-cells were separated by a Selemion DSV-N anion exchange membrane pretreated in 1 M NaCl solution. Three layers of carbon paper (SGL 39AA) baked at 400 °C overnight were used in each half-cell. The cell was cycled at a constant current of 30 mA cm^{-2}, followed by a constant charging voltage of 1.5 V and discharging voltage of 0.5 V until the current drops to 1 mA cm^{-2}.

Supporting Information

Supporting Information is available from the Wiley Online Library or from the author.

Acknowledgements

J.G. and K.A. contributed equally to this work. This research was supported by the National Science Foundation through grant CBET-1914543 and by U.S. DOE award DE-AC05-76RL01830 through PNNL subcontract 535264. K.A. was supported in part by U.S. DOE award DE-AC05-76RL01830 through PNNL subcontract 535264 and in part through the Natural Sciences and Engineering Research Council of Canada (NSERC) Postdoctoral Fellowship (PDF) program [application number PDF-557232-2021]. T.T. was supported by Japan Society for the Promotion of Science (JSPS) postdoctoral fellowship. T.Y.G. was supported in part by NSF-GRFP. The authors thank Dr. Shao-liang Zheng for single-crystal XRD analysis, and Jennifer Wang for mass spectrometry analysis. The authors also thank Dr. Emily Kerr, Daniel Pollack, Eliza Spear, Abdulrahman Alfaraidi, Eric Fell, Jordan Sosa, Dr. Robert Gustafson, and Dr. Martin Jin for valuable discussions.

Conflict of Interest

The authors declare no conflict of interest.

Data Availability Statement

The data that support the findings of this study are available from the corresponding author upon reasonable request.

Keywords

aqueous redox flow batteries, decomposition pathways, energy storages, metallorganics, posolytes

Received: December 12, 1912
Revised: December 12, 1912
Published online:

[1] L. Clarke, Y.-M. Wei, A. De La Vega Navarro, A. Garg, A. N. Hahmann, S. Khennas, I. M. L. Azevedo, A. Löschel, A. K. Singh, L. Steg, G. Strbac, K. Wada, Energy Systems, in *IPCC, 2022: Climate Change 2022: Mitigation of Climate Change. Contribution of Working Group III to the Sixth Assessment Report of the Intergovernmental Panel on Climate Change* (Eds: P. R. Shukla, J. Skea, R. Slade, A. Al Khourdajie, R. vanDiemen, D. McCollum, M. Pathak, S. Some, P. Vyas, R. Fradera, M. Belkacemi, A. Hasija, G. Lisboa, S. Luz, J. Malley), Cambridge University Press, Cambridge, UK and New York, NY, USA **2022**.
[2] O. Ellabban, H. Abu-Rub, F. Blaabjerg, *Renewable Sustainable Energy Rev.* **2014**, *39*, 748.
[3] J. Rugolo, M. J. Aziz, *Energy Environ. Sci.* **2012**, *5*, 7151.
[4] P. Leung, X. Li, C. Ponce de León, L. Berlouis, C. T. J. Low, F. C. Walsh, *RSC Adv.* **2012**, *2*, 10125.
[5] G. L. Soloveichik, *Chem. Rev.* **2015**, *115*, 11533.
[6] B. S. Jayathilake, E. J. Plichta, M. A. Hendrickson, S. R. Narayanan, *J. Electrochem. Soc.* **2018**, *165*, A1630.
[7] Y. K. Zeng, T. S. Zhao, L. An, X. L. Zhou, L. Wei, *J. Power Sources* **2015**, *300*, 438.
[8] N. H. Hagedorn, DOE/NASA/12726-24, NASA-TM-83677, United States **1984**.
[9] S. Roe, C. Menictas, M. Skyllas-Kazacos, *J. Electrochem. Soc.* **2015**, *163*, A5023.
[10] B. Huskinson, M. P. Marshak, C. Suh, S. Er, M. R. Gerhardt, C. J. Galvin, X. Chen, A. Aspuru-Guzik, R. G. Gordon, M. J. Aziz, *Nature* **2014**, *505*, 195.
[11] K. Lin, Q. Chen, M. R. Gerhardt, L. Tong, S. B. Kim, L. Eisenach, A. W. Valle, D. Hardee, R. G. Gordon, M. J. Aziz, M. P. Marshak, *Science* **2015**, *349*, 1529.
[12] D. G. Kwabi, K. Lin, Y. Ji, E. F. Kerr, M.-A. Goulet, D. De Porcellinis, D. P. Tabor, D. A. Pollack, A. Aspuru-Guzik, R. G. Gordon, M. J. Aziz, *Joule* **2018**, *2*, 1894.

[13] M. Wu, Y. Jing, A. A. Wong, E. M. Fell, S. Jin, Z. Tang, R. G. Gordon, M. J. Aziz, *Chem* **2020**, *6*, 1432.
[14] M. Wu, M. Bahari, E. M. Fell, R. G. Gordon, M. J. Aziz, *J. Mater. Chem. A* **2021**, *9*, 26709.
[15] E. S. Beh, D. De Porcellinis, R. L. Gracia, K. T. Xia, R. G. Gordon, M. J. Aziz, *ACS Energy Lett.* **2017**, *2*, 639.
[16] S. Jin, E. M. Fell, L. Vina-Lopez, Y. Jing, P. W. Michalak, R. G. Gordon, M. J. Aziz, *Adv. Energy Mater.* **2020**, *10*, 2000100.
[17] B. Hu, C. DeBruler, Z. Rhodes, T. L. Liu, *J. Am. Chem. Soc.* **2017**, *139*, 1207.
[18] T. Liu, X. Wei, Z. Nie, V. Sprenkle, W. Wang, *Adv. Energy Mater.* **2016**, *6*, 1501449.
[19] S. Jin, Y. Jing, D. G. Kwabi, Y. Ji, L. Tong, D. De Porcellinis, M.-A. Goulet, D. A. Pollack, R. G. Gordon, M. J. Aziz, *ACS Energy Lett.* **2019**, *4*, 1342.
[20] C. DeBruler, B. Hu, J. Moss, X. Liu, J. Luo, Y. Sun, T. L. Liu, *Chem* **2017**, *3*, 961.
[21] Y. Liu, M.-A. Goulet, L. Tong, Y. Liu, Y. Ji, L. Wu, R. G. Gordon, M. J. Aziz, Z. Yang, T. Xu, *Chem* **2019**, *5*, 1861.
[22] K. L. Hawthorne, J. S. Wainright, R. F. Savinell, *J. Electrochem. Soc.* **2014**, *161*, A1662.
[23] K. Gong, F. Xu, J. B. Grunewald, X. Ma, Y. Zhao, S. Gu, Y. Yan, *ACS Energy Lett.* **2016**, *1*, 89.
[24] X. Li, P. Gao, Y.-Y. Lai, J. D. Bazak, A. Hollas, H.-Y. Lin, V. Murugesan, S. Zhang, C.-F. Cheng, W.-Y. Tung, Y.-T. Lai, R. Feng, J. Wang, C.-L. Wang, W. Wang, Y. Zhu, *Nat. Energy* **2021**, *6*, 873.
[25] S. E. Waters, B. H. Robb, M. P. Marshak, *ACS Energy Lett.* **2020**, *5*, 1758.
[26] P. H. Daum, C. G. Enke, *Anal. Chem.* **1969**, *41*, 653.
[27] J. Luo, B. Hu, C. Debruler, Y. Bi, Y. Zhao, B. Yuan, M. Hu, W. Wu, T. L. Liu, *Joule* **2019**, *3*, 149.
[28] K. Lin, R. Gómez-Bombarelli, E. S. Beh, L. Tong, Q. Chen, A. Valle, A. Aspuru-Guzik, M. J. Aziz, R. G. Gordon, *Nat. Energy* **2016**, *1*, 1.
[29] A. Orita, M. G. Verde, M. Sakai, Y. S. Meng, *Nat. Commun.* **2016**, *7*, 13230.
[30] Z. Zhao, B. Zhang, B. R. Schrage, C. J. Ziegler, A. Boika, *ACS Appl. Energy Mater.* **2020**, *3*, 10270.
[31] C. X. Cammack, H. D. Pratt3rd, L. J. Small, T. M. Anderson, *Dalton Trans.* **2021**, *50*, 858.
[32] W. Ruan, J. Mao, S. Yang, Q. Chen, *J. Electrochem. Soc.* **2020**, *167*, 100543.
[33] B. A. G. Suzanne Ferrere, *J. Am. Chem. Soc.* **1998**, *120*, 843.
[34] Y. Ji, M. A. Goulet, D. A. Pollack, D. G. Kwabi, S. Jin, D. Porcellinis, E. F. Kerr, R. G. Gordon, M. J. Aziz, *Adv. Energy Mater.* **2019**, *9*, 1900039.
[35] Y. Jing, E. M. Fell, M. Wu, S. Jin, Y. Ji, D. A. Pollack, Z. Tang, D. Ding, M. Bahari, M.-A. Goulet, T. Tsukamoto, R. G. Gordon, M. J. Aziz, *ACS Energy Lett.* **2021**, *7*, 226.
[36] V. V. Avdeeva, A. V. Vologzhanina, L. V. Goeva, E. A. Malinina, N. T. Kuznetsov, *Z. Anorg. Allgem. Chem.* **2014**, *640*, 2149.
[37] N. Roznyatovskaya, J. Noack, K. Pinkwart, J. Tübke, *Curr. Opin. Electrochem.* **2020**, *19*, 42.
[38] R. Holze, *Electrochemical Thermodynamics and Kinetics*, Springer, Berlin, Germany **2007**.
[39] M. A. Goulet, L. Tong, D. A. Pollack, D. P. Tabor, S. A. Odom, A. Aspuru-Guzik, E. E. Kwan, R. G. Gordon, M. J. Aziz, *J. Am. Chem. Soc.* **2019**, *141*, 8014.
[40] Y. Jing, E. W. Zhao, M. A. Goulet, M. Bahari, E. M. Fell, S. Jin, A. Davoodi, E. Jonsson, M. Wu, C. P. Grey, R. G. Gordon, M. J. Aziz, *Nat. Chem.* Berlin, Germany **2022**, https://doi.org/10.1038/s41557-022-00967-4.
[41] L. J. Small, H. D. Pratt, T. M. Anderson, *J. Electrochem. Soc.* **2019**, *166*, A2536.
[42] V. P. Nemani, K. C. Smith, *J. Electrochem. Soc.* **2018**, *165*, A3144.
[43] E. M. Fell, D. D. Porcellinis, Y. Jing, V. Gutierrez-Venegas, R. G. Gordon, S. Granados-Focil, M. J. Aziz, (Preprint) ChemRxiv: 2022-zl7l6, unpublished: May **2022**.
[44] F. W. Joachim Demnitz, M. B. D'Heni, *Org. Prep. Proced. Int.* **1998**, *30*, 467.
[45] M. C. Young, E. Liew, J. Ashby, K. E. McCoy, R. J. Hooley, *Chem. Commun.* **2013**, *49*, 6331.
[46] N. E. Holubowitch, G. Nguyen, *Inorg. Chem.* **2022**, *61*, 9541.
[47] M. Park, E. S. Beh, E. M. Fell, Y. Jing, E. F. Kerr, D. Porcellinis, M. A. Goulet, J. Ryu, A. A. Wong, R. G. Gordon, J. Cho, M. J. Aziz, *Adv. Energy Mater.* **2019**, *9*, 1900694.
[48] H. Li, H. Fan, M. Ravivarma, B. Hu, Y. Feng, J. Song, *Chem. Commun.* **2020**, *56*, 13824.
[49] C. Zhang, Z. Niu, S. Peng, Y. Ding, L. Zhang, X. Guo, Y. Zhao, G. Yu, *Adv. Mater.* **2019**, *31*, 1901052.
[50] Y. Li, Z. Xu, Y. Liu, S. Jin, E. M. Fell, B. Wang, R. G. Gordon, M. J. Aziz, Z. Yang, T. Xu, *ChemSusChem* **2021**, *14*, 745.
[51] N. Poli, M. Schäffer, A. Trovò, J. Noack, M. Guarnieri, P. Fischer, *Chem. Eng. J.* **2021**, *405*, 126583.
[52] H. Bui, N. E. Holubowitch, *Int. J. Energy Res.* **2021**, *46*, 5864.